

See discussions, stats, and author profiles for this publication at: <https://www.researchgate.net/publication/260396614>

Co₃O₄@CeO₂ Core@Shell Cubes: Designed Synthesis and Optimization of Catalytic Properties

ARTICLE in CHEMISTRY - A EUROPEAN JOURNAL · APRIL 2014

Impact Factor: 5.73 · DOI: 10.1002/chem.201304109 · Source: PubMed

CITATIONS

12

READS

65

9 AUTHORS, INCLUDING:



Xiao Wang

Tianjin University

258 PUBLICATIONS 2,104 CITATIONS

SEE PROFILE



Da-Peng Liu

Chinese Academy of Sciences

42 PUBLICATIONS 1,083 CITATIONS

SEE PROFILE



Zhuo Wang

15 PUBLICATIONS 43 CITATIONS

SEE PROFILE



Hongjie Zhang

Chinese Academy of Sciences

428 PUBLICATIONS 11,874 CITATIONS

SEE PROFILE

Core@Shell Nanostructures

Co₃O₄@CeO₂ Core@Shell Cubes: Designed Synthesis and Optimization of Catalytic PropertiesJiangman Zhen,^[a, b] Xiao Wang,^[a, b] Dapeng Liu,^[a] Shuyan Song,^{*,[a]} Zhuo Wang,^[a, b] Yinghui Wang,^[a] Junqi Li,^[a, b] Fan Wang,^[a, b] and Hongjie Zhang^{*,[a]}

Abstract: Mastery of nanomaterial structure enables the control of its properties to enhance its performance for a given application. Herein, we demonstrate a fast and facile self-assembly method for the synthesis of a series of Co₃O₄@CeO₂ core@shell cubes, which are characterized by SEM, TEM, XRD, inductively coupled plasma mass spectrometry (ICP-MS), and X-ray photoelectron spectroscopy (XPS) analy-

ses. The results indicate that the thickness of the CeO₂ shell can be tuned through simple variation of the feeding molar ratio of Ce/Co. These Co₃O₄@CeO₂ core@shell cubes are used for catalytic CO oxidation and show good catalytic properties. Moreover, the relationship between the catalytic performance and the CeO₂ shell thickness is studied in depth to optimize the catalytic properties.

Introduction

Carbon monoxide (CO) is highly toxic, and poses serious problems for human health and industrial production, so the catalytic oxidation of CO is of great significance. Noble-metal-based catalysts always exhibit good catalytic performances for CO oxidation.^[1–8] For instance, Au-CeO₂,^[2] Au-TiO₂,^[3] and Pt-CeO₂^[5] hybrid catalysts have been studied widely. However, the high price of noble metals limits their further applications, so the development of novel “noble-metal-free” catalysts with well-controlled particle sizes, shapes, and structures as well as promising catalytic properties is quite an urgent issue to be addressed.

As one of the most important functional rare earth oxides, ceria (CeO₂) has been applied widely in catalysis, fuel cells, optical materials, gas sensors, and so forth. In particular, nanostructured ceria plays an active role in catalysis applications. Its catalytic properties are considered to originate from the Ce⁴⁺/Ce³⁺ redox cycle. Recently, a series of CeO₂-MO_x (M = metal, 1 ≤ x ≤ 3) mixed oxides have received more and more attention owing to their potential catalytic ability in CO oxidation.^[9–17] Among them, the CeO₂-CuO, CeO₂-MnO₂, CeO₂-Fe₂O₃, and

CeO₂-NiO systems are the most common ones.^[11–16] Typically, CeO₂-CuO catalysts obtained from the Cu₃(BTC)₂ (BTC: 1,3,5-benzene tricarboxylate) metal–organic framework precursor have shown high activities and selectivities in the preferential oxidation (PROX) reaction of CO in excess H₂.^[12] Ce-Mn binary oxide nanotubes, which were synthesized through a simple interfacial oxidation–reduction reaction exhibited high catalytic activities.^[14] CeO₂-NiO catalysts, prepared by using the combustion method, showed high activities as well as excellent stabilities in CO oxidation.^[15] Furthermore, a series of CeO₂-Fe₂O₃ composite catalysts were synthesized successfully through the coprecipitation method, and it was found that the Fe_{0.1}Ce_{0.9} composite showed the optimal catalytic performance.^[16]

Co₃O₄, as a low-cost, environmentally friendly, and chemically and thermodynamically stable metal oxide, also exhibits promising properties for CO oxidation.^[18–23] In this regard, Co₃O₄ was chosen as a catalyst in the form of CeO₂-Co₃O₄ heteronanocomposites (HNs). It is accepted that the CO oxidation process takes place at the interface between the CeO₂ and Co₃O₄ components.^[24] Therefore, increasing the interfacial area of CeO₂-Co₃O₄ HNs may be a feasible way to improve their catalytic performances. One way to optimize the fraction of the interfacial area of the two components is to prepare core@shell structures.^[25] To the best of our knowledge, there has been no successful work on Co₃O₄@CeO₂ core@shell nanostructures yet reported.

Here, we report a novel self-assembly method for the synthesis of high-quality Co₃O₄@CeO₂ core@shell HNs. Co₃O₄ cubes were synthesized first as the core,^[26] and this was followed by a controlled CeO₂ shell coating process. The thickness of this CeO₂ shell could be tuned easily by varying the feeding molar ratio of Ce/Co. Then, the as-obtained Co₃O₄@CeO₂ catalysts were studied in depth to find the optimal structure that showed the best catalytic performance for CO oxidation.

[a] J. Zhen, X. Wang, Dr. D. Liu, Dr. S. Song, Z. Wang, Dr. Y. Wang, J. Li, F. Wang, Prof. H. Zhang
State Key Laboratory of Rare Earth Resource Utilization
Changchun Institute of Applied Chemistry
Chinese Academy of Sciences
Changchun, 130022, Jilin (P. R. China)
Fax: (+86) 431-85698041
E-mail: songsy@ciac.ac.cn
hongjie@ciac.ac.cn

[b] J. Zhen, X. Wang, Z. Wang, J. Li, F. Wang
Graduate University of Chinese Academy of Sciences
Beijing 100039 (P. R. China)

Supporting information for this article is available on the WWW under <http://dx.doi.org/10.1002/chem.201304109>.

Results and Discussion

In the first step, we synthesized Co_3O_4 through a simple hydrothermal process. As shown in Figure 1 A and Figures S1 and S2

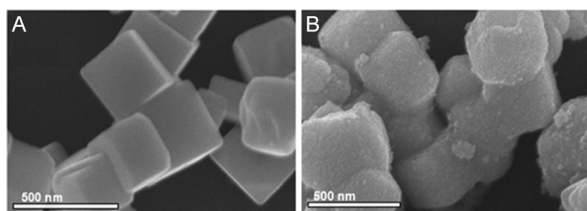


Figure 1. SEM images of a) Co_3O_4 cubes and b) $\text{Co}_3\text{O}_4@ \text{CeO}_2$ core@shell cubes.

(Supporting Information), the as-obtained Co_3O_4 particles were cubes with an average size of about 288 nm (Figure S2 also shows their size distribution histogram). After the addition of a certain amount of $\text{Ce}(\text{NO}_3)_3$ into the Co_3O_4 solution and heating at reflux for 2 h (Ce/Co feeding molar ratio: 8/12; experimental details are given in the Experimental section), the smooth surface of the Co_3O_4 cubes became rough (as shown in Figures 1B, S3, and S4). The high-resolution TEM image in Figure 2A shows that each Co_3O_4 cube was coated by a dense

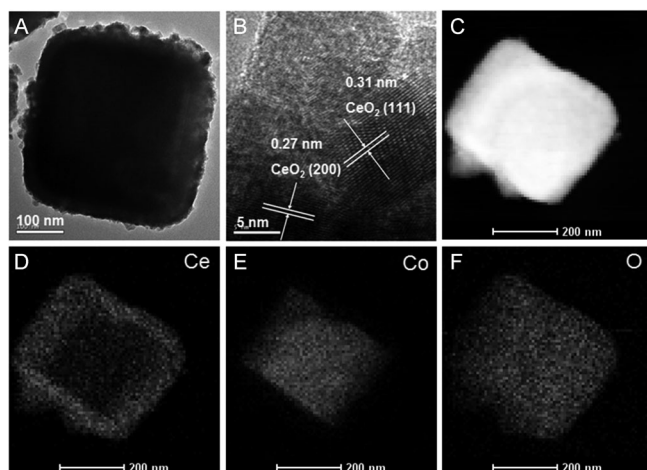


Figure 2. a,b) TEM images of $\text{Co}_3\text{O}_4@ \text{CeO}_2$ core@shell cubes, and c) the corresponding STEM image and d-f) EDX mapping analysis.

CeO_2 layer built up of hundreds of ultras small CeO_2 nanoparticles (NPs) self-assembled together. In Figure 2B, the lattice spacings of 0.31 and 0.27 nm correspond well to the characteristic (111) and (200) planes of fluorite-phase CeO_2 , respectively. The core@shell nanostructure could be distinguished further through mapping analysis (Figure 2C to 2F). It is seen clearly that the element Co is only present in the core position of the hybrid, and that Ce is distributed more widely, forming a compact shell.

Through simple variation of the amount of $\text{Ce}(\text{NO}_3)_3$, a series of $\text{Co}_3\text{O}_4@ \text{CeO}_2$ core@shell cubes could be synthesized by

using this self-assembly method. The as-obtained $\text{Co}_3\text{O}_4@ \text{CeO}_2$ core@shell cubes with different Ce/Co feeding molar ratios were designated as sample A (pure Co_3O_4), sample B (Ce/Co: 1/12), sample C (Ce/Co: 2/12), sample D (Ce/Co: 4/12), sample E (Ce/Co: 8/12), sample F (Ce/Co: 12/12), and sample G (pure CeO_2).

As shown in Figures 1, 3, and S3 to S12, samples B–F show similar core@shell cube structures, except that the monodis-

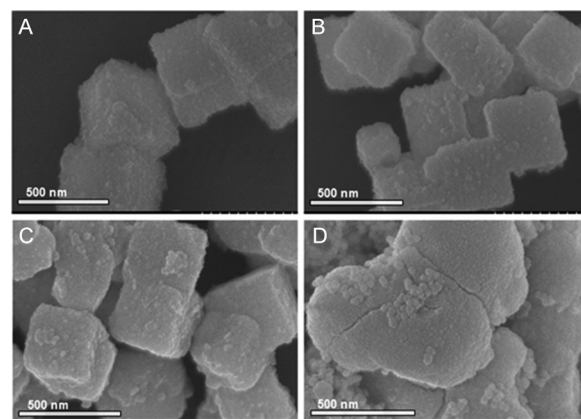
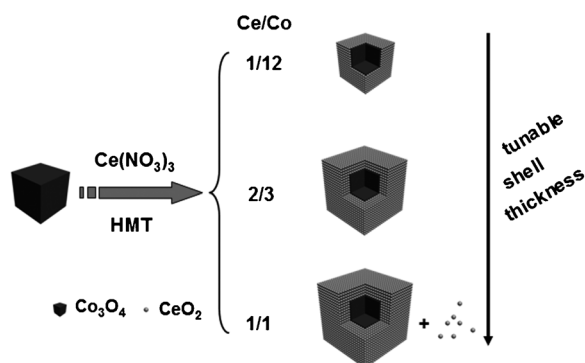


Figure 3. SEM images of the as-obtained samples B–F: a) sample B, b) sample C, c) sample D, d) sample F.

persed core@shell cubes began to stick together until a relatively large amount of $\text{Ce}(\text{NO}_3)_3$ was added (sample E, as shown in Figures 1B, S3, and S4). Upon further increasing the $\text{Ce}(\text{NO}_3)_3$ amount, the sticking phenomenon became more serious (sample F, as shown in Figures 3D, S11, and S12). Besides the aggregated cubes, some small CeO_2 NPs were scattered from the cubes. Samples B–F, which were synthesized with equal amounts of Co_3O_4 and different amounts of $\text{Ce}(\text{NO}_3)_3$, have different particle sizes. The greater the amount of $\text{Ce}(\text{NO}_3)_3$ used, the thicker the shell part of the $\text{Co}_3\text{O}_4@ \text{CeO}_2$ core@shell cubes. The average sizes of $\text{Co}_3\text{O}_4@ \text{CeO}_2$ core@shell cubes, estimated by the size distribution data, are 310, 330, 357, 390, and 433 nm for samples B–F, respectively, indicating that the corresponding average CeO_2 shell thicknesses become thicker and thicker from sample B to F. As shown in Figure S13, the as-obtained CeO_2 NPs are uniform with an average size of about 14 nm. Figure S14 shows the SEM images of samples A–G before calcination, and the SEM images of samples A–G after calcination are shown in Figures S2, S3, S5, S7, S9, S11, and S13, respectively. It is clear that the morphologies of the samples did not change after calcination. They maintained their size, shape, and hybrid nanostructure, indicating the good thermal stabilities of the samples. The abovementioned synthesis process is described in Scheme 1.

Figures 4A and 4B present the XRD patterns of samples A–G before and after calcination, respectively. There is no clear difference judged by XRD analysis. The peaks at $2\theta = 28.5^\circ$, 33.0° , 47.4° , 56.4° , 68.7° , 76.7° , and 78.9° can be indexed to the characteristic (111), (220), (220), (311), (400), (311), and (421) reflections of fluorite-phase CeO_2 , respectively (JCPDS No. 34-0394),



Scheme 1. Schematic process for preparation of samples B–F with different Ce/Co feeding molar ratios.

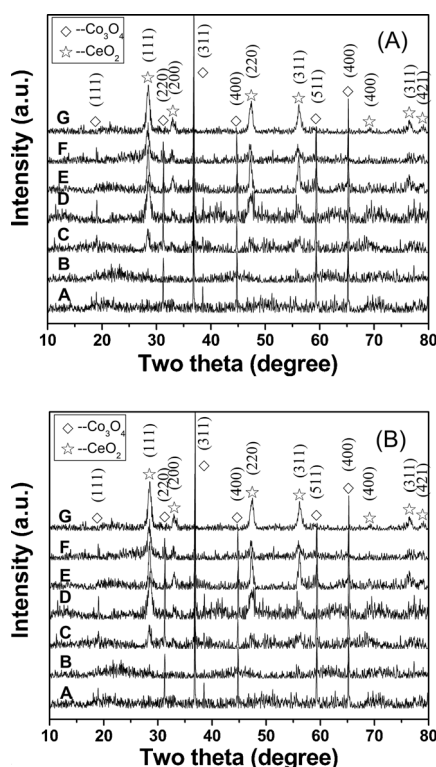


Figure 4. XRD patterns of samples A–G: a) before and b) after calcination.

and those at $2\theta = 19.0^\circ$, 31.3° , 36.8° , 44.8° , 59.3° , and 65.2° correspond well to the (111), (220), (311), (400), (511), and (400) reflections of spinel-phase Co_3O_4 , respectively (JCPDS No. 76-1802). The peaks related to CeO_2 are rather broad, but the Co_3O_4 peaks are sharp. This indicates that the CeO_2 NPs are much smaller than the Co_3O_4 cubes, which is consistent with the SEM and TEM characterizations.

XPS spectra were also obtained as shown in Figure S15. These confirm the presence of cerium in the hybrids, because the two peaks at 882.3 and 898.4 eV correspond to the Ce $3d_{5/2}$ and Ce $3d_{3/2}$ spin-orbit peaks of CeO_2 , respectively. As reported previously, the XPS curve of Co 2p shows two major peaks at

795.5 and 780.4 eV, corresponding to the Co $2p_{1/2}$ and Co $2p_{3/2}$ spin-orbit signals, respectively.^[27] As shown in Figure S15b, there are no clear Co signals in the binding energy range 775–810 eV. However, it is well known that the XPS characterization is only suitable for testing the superficial composition of samples, so the absence of Co peaks and the presence of Ce peaks confirms the core@shell structure of the as-obtained $\text{Co}_3\text{O}_4@\text{CeO}_2$ cubes, in accordance with the SEM and TEM analysis results. The Co and Ce contents were determined by ICP-MS. As shown in Table S1, the Ce contents are 4.64%, 8.31%, 15.79%, 25.23%, and 37.45% for samples B–F, respectively. Brunauer–Emmett–Teller (BET) gas-sorption measurements were performed to obtain the specific surface areas of the as-obtained $\text{Co}_3\text{O}_4@\text{CeO}_2$ core@shell cubes. The N_2 adsorption–desorption isotherms are shown in Figure S16. The BET specific surface areas are measured to be 3.0876, 9.3491, 8.2785, 7.1636, and $23.9178 \text{ m}^2 \text{ g}^{-1}$ for samples B–F, respectively.

The catalytic performances of samples A–G were investigated for the catalysis of CO oxidation. The CO conversion curves

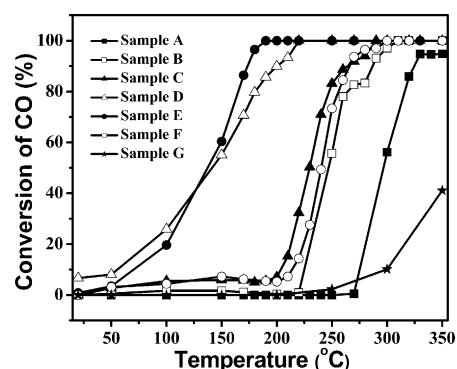


Figure 5. CO conversion curves of samples A–G.

are displayed in Figure 5. The T_{100} values (temperature for 100% CO conversion) are listed in Table 1 to compare the catalytic activities of the samples. In Figure 5, it is found that the T_{100} values of samples B–F (all five $\text{Co}_3\text{O}_4@\text{CeO}_2$ core@shell cubes) are below 350°C . For samples B–F, 100% CO conversion was obtained at 320 , 290 , 220 , 190 , and 300°C , respectively. Samples A and G showed almost no catalytic activity below 250°C . Upon a further increase in temperature, they began to

Table 1. Characteristics of $\text{Co}_3\text{O}_4@\text{CeO}_2$ core@shell cubes and their catalytic performances for CO oxidation.

Sample	CeO_2 theoretical content [mol %] ^[a]	CeO_2 theoretical content [mol %] ^[b]	Average size of $\text{Co}_3\text{O}_4@\text{CeO}_2$ core@shell cubes [nm] ^[c]	T_{100} [$^\circ\text{C}$] ^[d]
B	7.69	4.64	310	320
C	14.29	8.31	330	290
D	25	15.79	357	220
E	40	25.23	390	190
F	50	37.45	433	300

[a] Feed ratios of metal ion. [b] Determined by ICP-AES analysis. [c] Average size of $\text{Co}_3\text{O}_4@\text{CeO}_2$ core@shell cubes based on SEM and TEM results. [d] Temperature for 100% CO conversion (T_{100}).

show catalytic activities for CO oxidation. However, only 95% and 41.4% CO conversion was realized at 350 °C for samples A and G, respectively. As reported previously, the catalytic activities of CuO and NiO catalysts can be increased upon forming mixed oxides with CeO₂. This enhancement is attributed to the synergetic effects of CuO and NiO with CeO₂.^[10,14] The as-obtained Co₃O₄@CeO₂ core@shell cubes showed much higher catalytic activities than either Co₃O₄ or CeO₂, so it is reasonable to consider that the enhancement is caused by the synergistic effects between Co₃O₄ and CeO₂. Of all the samples, sample E showed the optimal catalytic performance. Next, a cycling test was performed to study the stability of sample E upon repeated tests in 1% CO gas (Figures S17 and S18). After ten successful cycles from 50 to 250 °C, sample E still maintained a 100% conversion rate of CO into CO₂ at 190 °C, and about 90% conversion at 170 °C.

For a further evaluation of its catalytic stability, sample E was characterized by TEM, SEM, and XRD analyses after the CO oxidation test. The TEM images of sample E are shown in Figure 6A and 6B. It is seen clearly that the structure of the

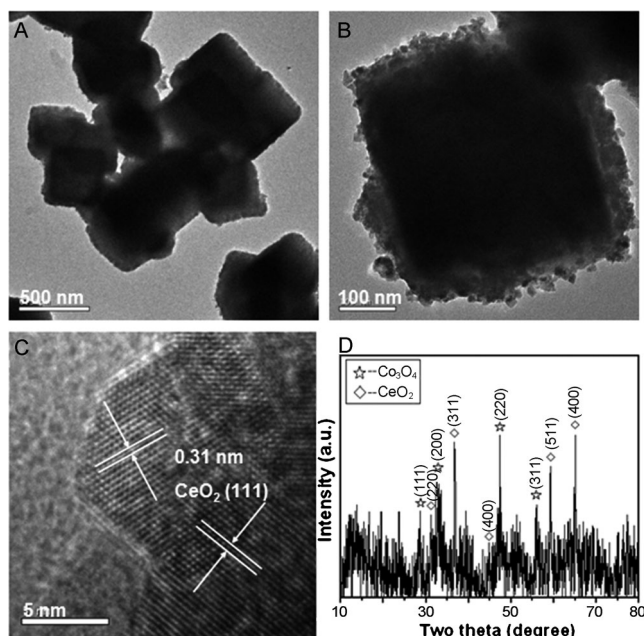


Figure 6. TEM images and XRD pattern of sample E after CO oxidation test.

Co₃O₄@CeO₂ core@shell cubes is retained quite well. CeO₂ NPs, which did not show significant changes in size and morphology, are still coated well on the Co₃O₄ cube. Figure 6C shows a high-resolution TEM (HRTEM) image of the CeO₂ NPs, which shows clearly that the lattice spacing of 0.31 nm corresponds well to the characteristic (111) plane of fluorite-phase CeO₂. This is consistent with the HRTEM characterization before the CO oxidation test. Figure 6D shows the XRD pattern of sample E after the CO oxidation test. There is no clear difference in the XRD results before and after the CO oxidation test, which indicates that the Co₃O₄@CeO₂ core@shell cubes are sufficiently stable during the catalytic CO oxidation process.

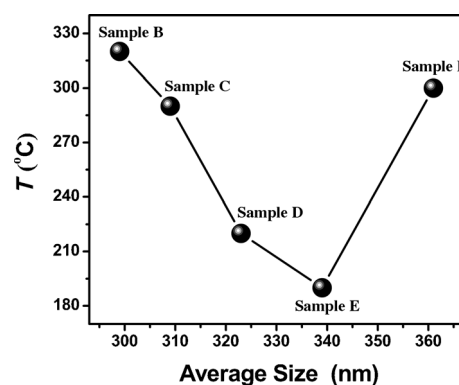


Figure 7. Relationship between average size of Co₃O₄@CeO₂ core@shell cubes and catalytic activities of samples B–F.

Figure 7 presents the relationship between T_{100} and the average size of Co₃O₄@CeO₂ core@shell cubes. First, from samples B–E, the catalytic activities of the Co₃O₄@CeO₂ core@shell cubes increased with increasing CeO₂ shell thickness up to an average size of 390 nm for the Co₃O₄@CeO₂ core@shell cubes, with sample E showing the best catalytic activity. With a further increase in CeO₂ shell thickness, the catalytic activity decreased (sample G). This suggests that the catalytic activities are highly dependent on the CeO₂ shell thickness. Sample E shows the best catalytic activity, and an increase or decrease in CeO₂ shell thickness causes a degradation of the catalytic performance.

Conclusion

In summary, we have demonstrated a fast and facile self-assembly method for the synthesis of Co₃O₄@CeO₂ core@shell cubes. To the best of our knowledge, this is for the first time these high-quality core@shell Co₃O₄@CeO₂ HNPs have been produced. The catalytic properties of the samples have been investigated systematically. The Co₃O₄@CeO₂ core@shell cubes show higher catalytic activities than either pure Co₃O₄ or CeO₂; this is attributed to synergistic effects between the two components, Co₃O₄ and CeO₂. The results suggest that the catalytic activities of the Co₃O₄@CeO₂ core@shell cubes depend strongly on the CeO₂ shell thickness. Sample E has an optimal CeO₂ shell thickness for the best catalytic activity, attaining 100% CO conversion at 190 °C. In addition, it shows good catalytic stability during the CO oxidation process. We believe that our Co₃O₄@CeO₂ core@shell cubes may be promising candidate catalysts for CO oxidation. Thus, this work supplies an efficient way to optimize the catalytic performance through simple control of the shell thickness, which will lead to further exploration of these kinds of heteronanocatalysts.

Experimental Section

Synthesis of Co₃O₄ cubes

Co₃O₄ was synthesized through a simple hydrothermal method as reported previously in the literature^[26] Co(NO₃)₂ (10 mmol) and NaOH (2.5 mmol) were dissolved in water (10 mL). The mixed reac-

tants were heated at 180 °C for 5 h and then allowed to cool to room temperature. The obtained products were washed with ethanol and water several times, and then dried at 60 °C.

Synthesis of Co₃O₄@CeO₂ core@shell cubes

Co₃O₄ cubes (50 mg) were dispersed ultrasonically in a mixed solution of water (20 mL) and ethanol (20 mL). Ce(NO₃)₃ (0.05 mmol) and hexamethylenetetramine (HMT) solution (2.5 mL, 0.02 g L⁻¹) were added in turn. Then, the temperature of the mixture was increased to 70 °C and kept under reflux for 2 h before being cooled to room temperature. The products were purified by centrifugation and washed once with water, then dried at 60 °C. Finally, the products were calcined in air at 400 °C for 3 h. The above experimental process was for the preparation of sample B. Samples C–F were prepared in a similar way, but with different amounts of Ce(NO₃)₃ and HMT. Ce(NO₃)₃ (0.1 mmol) and HMT solution (5 mL, 0.02 g L⁻¹) were used for the preparation of sample C; Ce(NO₃)₃ (0.2 mmol) and HMT solution (10 mL, 0.02 g L⁻¹) were used for sample D; Ce(NO₃)₃ (0.4 mmol) and HMT solution (15 mL, 0.02 g L⁻¹) were used for sample E; and Ce(NO₃)₃ (0.6 mmol) and HMT solution (20 mL, 0.02 g L⁻¹) were used for sample F.

Synthesis of CeO₂ NPs

Ce(NO₃)₃ (1 mmol) was dissolved in a mixed solution of water (20 mL) and ethanol (20 mL). Then, HMT solution (25 mL, 0.02 g L⁻¹) was added to the solution. The mixture was heated to 70 °C and maintained under reflux for 2 h before being cooled to room temperature. The products were purified by centrifugation and washed once with water, then dried at 60 °C. Finally, the products were calcined in air at 400 °C for 3 h.

Characterization

The X-ray diffraction patterns of the products were collected on a Rigaku-D/max 2500 V X-ray diffractometer with Cu_{Kα} radiation (λ = 1.5418 Å), with an operation voltage and current maintained at 40 kV and 40 mA. Transmission electron microscopic (TEM) images were obtained with a TECNAI G2 high-resolution transmission electron microscope operating at 200 kV. X-ray photoelectron spectroscopy (XPS) measurements were taken on an ESCALAB-MKII 250 photoelectron spectrometer (VG Co.) with Al_{Kα} X-ray radiation as the X-ray source for excitation. N₂ sorption isotherms were obtained at 77 K on an Auto-sorb-1 apparatus. Inductively coupled plasma (ICP) analyses were performed with a Varian Liberty 200 spectrophotometer to determine the Ce content.

Catalytic tests

The catalyst (25 mg) was placed in a stainless steel reaction tube. The CO oxidation catalytic tests were performed under conditions of 1% CO and 20% O₂ in N₂ at a fixed space velocity of 30 mL min⁻¹. The composition of the gas was monitored on-line by gas chromatography.

Acknowledgements

We are grateful for financial aid from the National Natural Science Foundation of China (Grant Nos. 21001101, 21071140,

51272249, 91122030, and 21210001), "863"-National High Technology Research and Development Program of China (Grant No. 2011AA03A407), and the National Natural Science Foundation for Creative Research Group (Grant No. 21221061).

Keywords: catalysis • CO oxidation • Co₃O₄@CeO₂ • core@shell • heteronanocomposite • nanostructures

- [1] C. Wang, H. F. Yin, S. Dai, S. H. Sun, *Chem. Mater.* **2010**, *22*, 3277–3282.
- [2] J. Qi, J. Chen, G. D. Li, S. X. Li, Y. Gao, Z. Y. Tang, *Energy Environ. Sci.* **2012**, *5*, 8937–8941.
- [3] S. F. Chen, J. P. Li, K. Qian, W. P. Xu, Y. Lu, W. X. Huang, S. H. Yu, *Nano Res.* **2010**, *3*, 244–255.
- [4] M. Cargnello, N. L. Wieder, T. Montini, R. J. Gorte, P. Fornasiero, *J. Am. Chem. Soc.* **2010**, *132*, 1402–1409.
- [5] X. Wang, D. P. Liu, S. Y. Song, H. J. Zhang, *J. Am. Chem. Soc.* **2013**, *135*, 15864–15872.
- [6] K. Yoon, Y. Yang, P. Lu, D. H. Wan, H. C. Peng, K. S. Masias, P. T. Fanson, C. T. Campbell, Y. N. Xia, *Angew. Chem. Int. Ed.* **2012**, *51*, 9543–9546.
- [7] A. Satsuma, M. Yanagihara, J. Ohyama, K. Shimizu, *Catal. Today* **2013**, *201*, 62–67.
- [8] R. Güttel, M. Paul, C. Galeano, F. Schuth, *J. Catal.* **2012**, *289*, 100–104.
- [9] L. H. Reddy, G. K. Reddy, D. Devaiah, B. M. Reddy, *Appl Catal A-Gen* **2012**, *445*, 297–305.
- [10] S. Varghese, M. G. Cutrufello, E. Rombi, C. Cannas, R. Monaci, I. Ferino, *Appl Catal A-Gen* **2012**, *443*, 161–170.
- [11] A. Hornés, A. B. Hungria, P. Bera, A. L. Camara, M. F. Garcia, A. M. Arias, L. Barrio, M. Estrella, G. Zhou, J. J. Fonseca, J. C. Hanson, J. A. Rodriguez, *J. Am. Chem. Soc.* **2010**, *132*, 34–35.
- [12] F. Zhang, C. Chen, W. M. Xiao, L. Xu, N. Zhang, *Catal. Commun.* **2012**, *26*, 25–29.
- [13] S. H. Zeng, Y. Wang, K. W. Liu, F. R. Liu, H. Q. Su, *Int. J. Hydrogen Energy* **2012**, *37*, 11640–11649.
- [14] G. Z. Chen, F. Rosei, D. L. Ma, *Adv. Funct. Mater.* **2012**, *22*, 3914–3920.
- [15] S. Mahammadunnisa, P. M. K. Reddy, N. Lingaiah, C. Subrahmanyam, *Catal. Sci. Technol.* **2013**, *3*, 730–736.
- [16] H. Z. Bao, X. Chen, J. Fang, Z. Q. Jiang, W. X. Huang, *Catal. Lett.* **2008**, *125*, 160–167.
- [17] S. H. Zeng, W. L. Zhang, S. L. Guo, H. G. Su, *Catal. Commun.* **2012**, *23*, 62–66.
- [18] Y. J. Feng, L. Li, S. F. Niu, Y. Qu, Q. Zhang, Y. S. Li, W. R. Zhao, H. Li, J. L. Shi, *Appl Catal B-Environ* **2012**, *111*, 461–466.
- [19] H. Tüysüz, M. Comotti, F. Schuth, *Chem. Commun.* **2008**, 4022–4024.
- [20] C. B. Wang, C. W. Tang, S. J. Gau, S. H. Chien, *Catal. Lett.* **2005**, *101*, 59–63.
- [21] Y. Z. Wang, Y. X. Zhao, C. G. Gao, D. S. Liu, *Catal. Lett.* **2008**, *125*, 134–138.
- [22] X. W. Xie, Y. Li, Z. Q. Liu, M. Haruta, W. J. Shen, *Nature* **2009**, *458*, 746–749.
- [23] Y. B. Yu, T. Takei, H. Ohashi, H. He, X. L. Zhang, M. Haruta, *J. Catal.* **2009**, *267*, 121–128.
- [24] J. Y. Luo, M. Meng, Y. Q. Zha, L. H. Guo, *J. Phys. Chem. C* **2008**, *112*, 8694–8701.
- [25] T. Mitsudome, Y. Mikami, M. Matoba, T. Mizugaki, K. Jitsukawa, K. Kaneda, *Angew. Chem. Int. Ed.* **2012**, *51*, 136–139.
- [26] X. L. Xiao, X. F. Liu, H. Zhao, D. F. Chen, F. Z. Liu, J. H. Xiang, Z. B. Hu, Y. D. Li, *Adv. Mater.* **2012**, *24*, 5762–5766.
- [27] B. Varghese, T. C. Hoong, Z. Yanwu, M. V. Reddy, B. V. R. Chowdari, A. T. S. Wee, T. B. C. Vincent, C. T. Lim, C. H. Sow, *Adv. Funct. Mater.* **2007**, *17*, 1932–1939.

Received: October 21, 2013

Published online on February 26, 2014